Supplemental Data

Consequences of Motor Copy Number

on the Intracellular Transport of

Kinesin-1-Driven Lipid Droplets

George T. Shubeita, Susan L. Tran, Jing Xu, Michael Vershinin, Silvia Cermelli, Sean L. Cotton, Michael A. Welte, and Steven P. Gross

1) Is kinesin-1 the only plus-end motor on lipid droplets?

We find that kinesin-1 is absolutely required for net plus-end transport of droplets and for motion of individual droplets. We performed four independent tests to distinguish if kinesin's role in droplet transport is direct or indirect. First, kinesin-1 is physically present on droplets. Second, acute inhibition of kinesin-1 with antibodies quickly abolishes net plus-end transport. Third, partially functional kinesin-1 results in reduced transport velocities of droplets, in an allele-specific manner. Fourth, mere reduction in kinesin-1 levels causes reduced droplet stall forces. Together, these results very strongly suggest that kinesin's role in droplet transport is direct; we conclude that kinesin-1 powers plus-end motion of lipid droplets.

Bidirectionally moving cargos are typically thought to engage only a single type of motor for each direction of transport. To our knowledge, no cases are known in which several different plus- or minus-end motors cooperate on a single bidirectional cargo. However, during intraflagellar transport in *C. elegans*, two distinct plus-end motors work together to transport uni-directionally moving IFT particles (Pan et al., 2006). Following this precedent, it is therefore conceivable that the plus-end transport of lipid droplets employs an as-yet unidentified Kin-X in addition to kinesin-1. Although the current data cannot exclude that such a Kin-X exists, we have no evidence supporting such a hypothesis. Further, our data put severe limits on the properties of such a hypothetical motor.

The activity of Kin-X would have to depend entirely on kinesin-1, since in the absence of Khc there is no motion. More restrictively, Kin-X activity would even depend closely on kinesin-1 levels since reduced kinesin-1 expression results in reduced stall forces. Kinesin-1 and Kin-X would thus display the same coupling that we discovered between Dynein and kinesin-1: the amount of Kin-X engaged would be limited by the amount of kinesin-1 available. Such complete interdependence of two plus-end motors would be quite different from the situation for *C. elegans* intraflagellar transport where the two motors can function independently and either motor supports vigorous transport in the absence of the other.

To circumvent complications due to coupling, we employed two distinct approaches to perturb kinesin-1 without abolishing Dynein activity and thus without causing a general breakdown of motor assembly. First, we generated germ-line clones of the hypomorphic Khc alleles Khc^{23} and Khc^{17}; these GLC embryos display bidirectional motion of droplets. Second, we inhibited kinesin-1 acutely with antibodies, a treatment which induces net minus-end

transport and thus does not abolish Dynein activity. In both cases, Kin-X would presumably also remain active. However, this putative activity is not sufficient to support net plus-end droplet motion (Figs. 1D, 2D). This suggests that kinesin-1 dominates the plus-end motion of droplets and that, if there were to be a Kin-X, on its own it could at most make a restricted contribution to transport.

We clearly do not yet know all the components that make up the droplet transport machinery. However, even if a hypothetical Kin-X were among the unknown components, the key findings of this paper remain valid. First, we conclude that single cargos can simultaneously engage multiple copies of kinesin-1. This point is demonstrated by the fact that stall forces on droplets change when Khc expression levels are altered. Second, we explore a key, untested assumption of other studies concerning motor-function in vivo, namely that there is a tight relationship between the number of active motors on cargos and certain parameters of motion. In particular, we find that a reduction in the number of engaged motors, confirmed biochemically and reflected functionally in the decrease in stall forces, does NOT alter travel velocities. This finding casts grave doubts on the validity of a widespread strategy of inferring motor number on cargos, that is, on using variations in travel velocities to infer variations in stall forces and therefore implicitly in the number of active motors (see also section 7 below). Further, more motors do not move the cargo further, casting potential doubt on a generally assumed regulatory mechanism, whereby transport is regulated by controlling the number of motors bound to the cargo. Obviously, in the extreme case (i.e. entirely removing motors from the cargo) such a scheme will work, but our results suggest that more subtle changes in the number of cargo-bound motors may have relatively little effect on the overall transport of the cargos.

2) Kinesin-1 has roles in early embryos beyond droplet transport

Mutants affecting kinesin-1 function display altered microtubule organization (apical bundling of microtubules and/or microtubule length control; Fig. 2A) and abnormal cellularization. Whether these defects are directly caused by lack of kinesin-1 activity remains to be established; intriguingly, injection of the function-inhibiting anti-Khc antibody disrupts cellularization (SLT and MAW, unpublished).

3) Lipid droplets are moved by multiple motors
A number of lines of evidence presented in the paper support the hypothesis that droplets are moved by multiple kinesin-1 motors. First, in Khc^{27} heterozygotes, both the amount of kinesin-1 on droplets and the average force required to stall droplets are decreased relative to the wild type. As moving droplets have at least one kinesin-1, the higher forces in the wild type must represent the action of multiple motors per droplet. Second, the distribution of stall forces reveals at least three force states in the wild type (Fig. 3C). Since stall forces in vitro are additive, we propose that these force states represent one motor (2.6 pN peak), two motors (5.2 pN peak) and three or more motors (escapers), respectively. If these three force states instead represented distinct functional states of a single motor, the same three states would still be expected when kinesin-1 levels are reduced. However, in Khc^{27} heterozygotes, the highest force state (escapers) is essentially absent and the lowest force state is much more predominant. A similar shift in force states is observed in vitro when motor numbers are reduced (Vershinin et al., 2007).

Our previous population measurements of stall forces suggested that some droplets are moved by up to five motors (Welte et al., 1998). Those studies had focused on the upper end of the force distribution because they required estimates of the force required to stop all droplets.

For the studies reported here, we employed a relatively small trap stiffness, in order to resolve stalls at low forces. As a result, cargos moved by more motors frequently escape the trap.

4) Variability of stall force measurements

The width of the peaks in the stall force histogram (Fig 3C) is ~ ± 1.5 pN. This data is approximately consistent with what is observed in vitro, taking into account the additional sources of uncertainty in vivo. For instance, for a single kinesin-1, the width of the peak for our in vitro data is about ±1.6 pN (Vershinin et al., 2007). The width of a distribution typically changes with the square root of the mean of the distribution, so since the mean in vivo stall is approximately ½ of the kinesin stall in vitro, if everything were to be the same, we would expect the in vivo distribution to have a width of approximately $1.6/\sqrt{2} = 1.13$ pN. However, there are a number of factors contributing to the width of the distribution in vivo not present in vitro, including a variety of sources of error such as variation in cargo size (that we correct for, but still provides error), and slight errors in determination of the position of the optical trap (it is fixed in the in vitro measurements, but must be moved to be over the droplet in the in vivo measurements). We believe that these additional sources of error account for the increased ~0.37 pN of width of the peak.

Although there is more uncertainty, this in no way invalidates the measurements of the centers of the peaks. By fitting to a sum of Gaussians, with unconstrained centers, the relative contribution of the different populations is still determined since the peaks are well separated. The chi-squared analysis mentioned in the main text suggests that fitting with two Gaussians is a much better model of the data than only one. Thus, we can indeed recover the approximate relative number of two-motor versus one-motor stall events, and the stall force can be used to estimate the number of active motors.

5) Measured versus actual mean stall force

In the main text, we show that in wild-type embryos the mean force to stall a plus-end moving droplet is approximately 4 pN, while in the $Khc^{27}/+$ embryos (where there is half as much kinesin per droplet), the stall force is approximately 2.4 pN. This reflects a force reduction of ~40%, less than the 50% decrease one might naively expect from a 50% reduction in the number of motors. We hypothesize that this apparent discrepancy is due to the fact that many lipid droplets escape the trap and do not contribute to the calculation of the average stall force, since their stall force is not measured. This underestimate of the average stall force is less severe for lipid droplets in $Khc^{27}/+$ embryos since they are moved by fewer motors than in the wild type, and we observe fewer that escape the trap. Thus, the average stall force we measure will be closer to the true average stall force for $Khc^{27}/+$ than for wild-type droplets.

6) Why are stall forces in vivo lower than kinesin-1 stall forces in vitro?

We speculate that in vivo cofactors exist that can modulate kinesin's force output. Such co-factors could take a number of forms. For instance, there could be currently unknown proteins that bind to the motors, and directly alter their force production. However, a second scenario (which we favor) is that there are additional linkages between the cargo and the microtubule that effectively oppose motion, so that the "stalling force" we measure includes the motor(s) working against such linkages. We can imagine two such classes of linkages. First, the opposite motors themselves could provide drag. Such a scenario is consistent with recent theoretical work (Müller

et al., 2008), and will need to be carefully investigated in the future. Second, non-motor molecules might link droplets to the microtubules and resist motion. If these linkages do not slide freely along the tracks, but act as brakes, they would provide an opposing load that reduces the effective force generated by kinesin. One candidate for such a linkage is Dynactin since it has both cargo- and microtubule-binding domains (Culver-Hanlon et al., 2006). If kinesin's single-molecule stall force in vivo is the same as in vitro (5 pN), the applied load due to such brakes (~2.4 pN) would slow down kinesin only ~15% (Schnitzer et al., 2000).

Stall force measurements are insensitive to viscous drag because they are performed at zero cargo velocity. The drag due to the proposed linkages is potentially different, because the Dynactin-microtubule interaction is a protein-protein interaction, and it is a priori unclear how it changes with velocity. For instance, it is possible that at very low velocities, it is a stronger interaction (more time to make bonds) but at higher velocities it is weaker (bonds do not have time to re-form). Thus, it could in principle either be constant, independent of velocity, or could have a stronger effect at lower velocities. This is different from viscosity, where the magnitude of the force increases linearly with increasing velocity.

7) Relationship between cargo velocity and the number of engaged motors

Currently, the hypothesis that 'in vivo, more motors move a cargo more rapidly' is quite popular (see e.g. (Hill et al., 2004; Kural et al., 2005; Levi et al., 2006)). This proposal is based on the *in-vitro* observation that motors slow down if they experience a significant load. By assuming that the viscous drag cargos experience is significant compared to the stall force of the motors moving them, these studies use observed velocity as a proxy for the number of engaged motors. However, there are three difficulties with this approach. First, motors are enzymes, and enzymatic rates (and hence motor velocity) might vary due to multiple other reasons (e.g., phosphorylation, the presence or absence of regulatory factors). Second, cytosolic drag may not be as high as assumed; for instance, our recent estimate of drag force opposing motor motion in *Drosophila* embryos revealed it to be relatively small (G.T.S. et al., unpublished data). Finally, even if drag is high, how a cargo driven by multiple motors reacts to such drag is not straightforward (Kunwar et al., 2008). Thus, a cargo's velocity does not necessarily reflect the number of motors moving it (see also (Martinez et al., 2007) for additional pitfalls associated with velocity-based estimation of the number of engaged motors). Therefore, until the studies presented in this manuscript, there had not be a well-controlled set of experiments to test to what extent variation in the number of engaged motors plays a role in determining cargo velocity in vivo.

The data in the main text show that for lipid droplets a reduction in motor numbers (from wild type to Khc^{27}/+) does NOT result in a decrease in cargo velocity. In contrast, droplets in the mutant move ~5.5% faster than droplets in the wild type. While the magnitude of the effect is relatively small, it has great bearing on the mechanism underlying transport. Our automated tracking and analysis is remarkably reproducible, and the increase in velocity reported here is well outside of our noise. To eliminate the possibility that the difference was due to embryo-to-embryo variation, we did additional recordings and analysis. We ended up with two complete data sets for wild-type embryos (each one with 5 embryos, and with the mean velocity in each set representing approximately 190 independent velocity measurements). We also had two complete data sets for Khc^{27}/+ embryos (each one with 8 embryos, and with the mean velocity in each set representing approximately 170 independent velocity measurements). The mean plus-end velocities for the two wild-type sets were 552 ± 13 nm/s and 555 ± 11nm/s, respectively. For the

Khc²⁷/+ embryos, the mean plus-end velocities for the two sets were 594 ± 11 nm/s and 582 ± 12 nm/s, respectively. Thus, comparing groups of ~8 embryos leads to significant confidence that the difference is real.

This surprising result—that fewer motors move slightly faster—is explained by a new theoretical model developed independently (Kunwar et al., 2008). This model incorporates the experimental *in-vitro* observation that under low load kinesin's processivity (mean travel) is decreased, but its velocity is not (Schnitzer et al., 2000). Because velocity is unaffected, motors do not clump on the microtubule, even when attached to the cargo at a single point. Thus, the load is not shared equally between all motors but is instead supported mostly by the leading motor. The increased load on the leading motor will cause it to detach more frequently from the microtubule than the rearward motors. When it does, the cargo's center of mass moves backwards since – due to thermal noise – it fluctuates around where the motors attach to the track. These frequent small backward motions are predicted to decrease the cargo's average velocity by approximately 6% relative to the velocity of cargos moved by one motor.

Over the likely range of cytosolic viscosities, the model predicts that cargos moved by two, three or four motors display approximately the same velocity; only for one-motor cargos is there a significant velocity change. Since droplets in *Khc²⁷*/+ embryos move faster than in the wild type, this adds additional support to the notion that droplets in *Khc²⁷*/+ embryos are predominantly transported by a single kinesin.

Although the theoretical model is based on the in vitro properties of kinesin-1, the underlying assumptions are rather generic and likely apply to other motors. In particular, we propose that Cytoplasmic Dynein behaves similarly since we observe a decrease in minus-end droplet velocities when more motors are engaged (Fig. 5E, bottom).

8) Robustness of transport

Net droplet transport is surprisingly robust: All wild-type embryos display clearing in Phase II and clouding in Phase III, a pattern preserved even when kinesin-1 levels are reduced in the *Khc²⁷*/+ embryos (Fig. 5F, movie S7). Initially we suspected that robustness of transport might be due to feedback mechanisms that keep the number of engaged motors constant, regardless of the *Khc* dosage (e.g. via transcriptional and post-transcriptional regulation of kinesin-1 levels). No such regulatory mechanisms appear to act since a reduction from two to one copy of the *Khc* gene resulted in a halving of the number of engaged motors. Our data point to two possibilities how robustness might be achieved.

First, the mean droplet travel distance (~ 600 nm) is smaller than the ~1000 nm expected for the single motor. We therefore hypothesize that the switch mechanism, rather than single-motor processivity, terminates runs even for single motor-driven droplets. We speculate that this may reveal a design principle of bidirectional transport such that it is robust to fluctuations in gene expression.

Second, coupling might improve the robustness of transport under conditions where coordination of opposite-polarity motors breaks down. There is indirect evidence that such breakdown of coordination may occur transiently even in the wild type (e.g. the short-slow runs discussed in (Gross et al., 2000)). If opposite motors are evenly balanced, such brief failures in coordination result in little net motion. If opposite motors were not balanced, then every time coordination was lost, the stronger set of motors would overwhelm the weaker set, strongly biasing transport in the stronger direction, regardless of the action of the switch mechanism.

Supplemental Experimental Procedures

Fly strains and genetics

Oregon R was used as the wild-type stock. *Khc* germ-line clones were generated as previously described (Serbus et al. 2005): *yw P{hs-FLP}; P{w⁺, FRT}42B P{ovo^{D1}}55D/CyO* males were crossed to females of one of following genotypes: (1) *w; P{w⁺, FRT}42B Khc²⁷/CyO* or (2) *w; P{w⁺, FRT}42B Khc¹⁷ Bc Elp px/CyO* or (3) *w; P{w⁺, FRT}42B Khc²³/CyO* to produce *yw P{hs-FLP}; P{w⁺, FRT}42B Khc^{27,17,or 23}/ P{w⁺, FRT}42B P{ovo^{D1}}55D* female larvae. Second-instar larvae were heat shocked once for 2 hours in a 37°C water bath. *Klc* germ-line clones were generated using a similar scheme (Palacios and St Johnston, 2002) by crossing *yw P{hs-FLP}; P{w⁺, FRT2A} P{ovo^{D1}}/TM3* males to *w; P{w⁺, FRT2A} Klc^{8ex94}/TM3* females. A *Khc⁺* transgene (Saxton et al., 1991) was used to express wild-type Khc and rescue *Khc* GLCs; this transgene has been variously called *PK4C, P{khc⁺}, P{Khc^{+t7.5}}* or *P{Khc^{+t7.5}}^{PK4C}* and is referred to in the text as *P{Khc⁺}*.

Antibody injections

For antibody injections, antibodies were processed as previously described (Serbus et al., 2005). 50 µg of antibodies (either rabbit anti-Khc (Cytoskeleton AKIN01-A) or rabbit anti-chicken (Jackson Immunology)) were first concentrated with Microcon filters (Amicon YM-30) and then dialyzed in a Slide-A-Lyzer Mini Dialysis Unit 10000 MWCO (Pierce) against 1 Liter of PBS (6 hours at 4°C). Final antibody concentrations were ~2-3 µg/µl. Embryos were prepared for injection using standard procedures (e.g., as in (Gross et al., 2003)).

According to the manufacturer, AKIN01-A was raised against the N-terminal 685 aa of *Drosophila* Khc and reacts only poorly even with the human homolog. This antibody has been used widely as a specific probe for *Drosophila* Khc in both western and immunofluorescence analyses (Duncan and Warrior, 2002; Brendza et al., 2002; Stowers et al., 2002; Ogden et al., 2003; Stegman et al. 2004). For example, injection of this antibody has been used to specifically inhibit the kinesin-1-driven cytoplasmic streaming in *Drosophila* oocytes (Serbus et al, 2005); this treatment resulted in phenotypes that mimic those obtained when kinesin-1 is inhibited genetically (Serbus et al, 2005). To specifically address if there is cross-reactivity with other proteins in early embryos, we employed this antibody for western analysis of various genotypes. In addition to the major Khc band just above 100 kDa, there are a number of additional bands. However, these bands are all dependent on Khc: First, no bands are detected in *Khc²⁷* germ-line clone embryos, even with very long exposures (Figs. 1C, S2D). In particular, note that this lane has no bands in the molecular weight range corresponding to the size of kinesin-2 motor subunits (76-88 kDa). Second, the bands we can detect are entirely dependent on the copy number of Khc: they increase and decrease in accordance with how many copies (endogenous genes or transgenes) of Khc are present in the mothers producing those embryos. We conclude that all of these bands represent Khc (presumably various degradation products) and that the antibody is very specific.

Immunolocalization and microscopy

Yolk vesicles, Klar and DNA were detected as previously described (Gross et al., 2003; Guo et al., 2005), using yolk autofluorescence, Klar-M immunostaining and Hoechst 33258, respectively. Embryo centrifugation was performed as described (Guo et al., 2005). To visualize

microtubules, dechorionated embryos were fixed with a 1:1 mixture of heptane and 19.5% formaldehyde/2.5% methanol/1xPBS for 30 minutes, devitellinized and blocked as described (Sisson et al., 2000). Embryos were incubated overnight with monoclonal antibody E7 against β tubulin (Developmental Studies Hybridoma Bank, University of Iowa; this antibody was originally developed by M. Klymkowsky) at 1:32.000 dilution, followed by Alexa 488-conjugated goat anti-mouse IgG at 1:8000. Images in Figs. 1D, 1E and 2A were acquired on a Leica TCS SP2 confocal microscope; all other micrographs were acquired on a Nikon Eclipse E600 fluorescence microscope with one of two Spot Insight cameras (models QE or 4MP, Diagnostic Instruments). For movie S7, embryos were dechorionated by hand and mounted in halocarbon oil under a coverslip supported by spacers. Brightfield images were acquired every minute and processed identically with Adobe Photoshop. To compare clearing progress at similar stages of embryogenesis, image sequences were aligned such that the frames representing the midpoint of cellularization (when membranes reach the basal tip of the nuclei) are synchronized for all three genotypes.

Western analysis

To analyze Khc levels in intact embryos, embryos were heat fixed as described (Guo et al., 2005), visually sorted by developmental stage and prepared for SDS-PAGE by boiling in 1x Laemmli buffer. Electrophoresis, transfer to PVDF membranes and immunodetection were performed as previously described (Guo et al., 2005; Welte et al., 2005), using anti-Khc at a dilution of 1:1000. Unless otherwise noted, proteins extracted from 10 embryos were loaded per lane, and equal loading was confirmed by staining membranes with Coomassie Blue. For the western in Fig. 1B, Phase II embryos were used in most instances; for the Khc^{27} GLC lane, we used embryos of varying ages because the yield of such embryos is low. This approach allows a valid comparison to the other genotypes as Khc levels do not vary during early embryogenesis in the wild type (Fig. S2B, and data not shown). To analyze proteins associated with lipid droplets, droplets were biochemically purified as described (Cermelli et al., 2006), and 50 μg protein of the droplet preparation or the starting embryo lysate were subjected to western analysis as above. Antibodies used: anti-Khc at 1:1000, anti-Klc (Gindhart et al., 1998) at 1:1000, anti Cdic (Chemicon MAB1618; see (Welte et al., 2005)) at 1:1000.

Lipid-droplet tracking and track analysis

Quantification of droplet motion was performed in Phase II during the clearing process, where droplets are on average moving toward the embryo center. As clearing is ongoing, not all droplets have cleared yet and some can be tracked. High-magnification images of embryos were recorded at 30 frames/second from the DIC microscope images to reveal lipid-droplet motion. Droplets were scored as moving in the plus- or minus-end direction if they moved away from or towards the surface of the embryo, respectively. Droplet trajectories were determined as previously (Gross et al., 2000; Welte et al., 1998) via a custom template matching algorithm (Carter et al., 2005) for particle tracking. To eliminate potential selection bias, all tracking was performed algorithmically and identically in all cases. Trajectories were produced by assembling a list of consecutive particle locations based on their displacements between adjacent frames and confidence levels of the template match. Only tracks of 20 frames or longer (>600 ms long) were used. The details of the template matching and tracking algorithm will be published elsewhere. The resulting tracks were parsed into constant-velocity segments and consecutive segments with motion in the same direction were grouped into runs (Petrov et al., 2007), i.e. runs are records of

motion from one reversal of direction to the next. Run-length distributions and velocities were calculated from at least 8 embryos per genotype, with on average 30 ± 5 droplets tracked per embryo. Run-length distributions were fit by two exponential decays as detailed previously (Gross et al., 2000). The two decay lengths (D_1 and D_2) characterize the short and long run lengths, respectively. Both decay lengths as well as the average run length (D_{avg}) are shown in Fig. 5A-D. Velocities shown in Fig. 5E are for runs longer than 500 nm.

To calculate the Mean square displacement (MSD) (Fig. 2F), we chose a representative embryo for each genotype and used all tracks whose duration exceeded 200 video frames. For each track, we computed the MSD curve:

$$MSD(n\Delta t) = \frac{1}{N-n}\sum_{m=1}^{N-n}\left[\vec{r}(m+n)-\vec{r}(m)\right]^2$$

where r(n) is the two-dimensional position of the tracked particle in frame n ($n \geq 1$ and $n \leq N/2$). The factor of $\Delta t = 0.033$ sec was used to convert the frame numbers above into real time. The first 100 points of the resulting curves were averaged ($n_{WT} = 37$ and $n_{Khc27\,GLC} = 44$) and plotted as a function of time.

Force measurements

Experimental details of the stall-force measurements on individual lipid droplets will be published elsewhere (G.T.S. et al., unpublished data). Briefly, an advanced optical trap setup was built atop an inverted optical microscope (Nikon TE 2000). For fast and precise alignment of the trap with the position of the lipid droplet, a computer-controlled piezoelectric stage-mounted mirror (Mad City Labs) was used in conjunction with a fast single-particle tracking program capable of real-time tracking of particles at rates exceeding 30 frames/sec (Carter et al., 2005). At the click of the mouse on the CCD camera image of a moving lipid droplet, the program determines the droplet's position with an accuracy of a few nanometers, triggers the piezo-driven mirror to move to that position and opens the shutter to trap the droplet. The position of the droplet in the trap was tracked at 30 frames/sec using the camera image. Upon projecting the resulting trace along the direction of droplet motion (microtubule), traces of position as a function of time similar to those presented in Fig. 3 were constructed. A cargo was scored as stalled if it remained stationary out of the center of the trap for at least 0.35 sec.

The procedure we used to calibrate the trap for in vivo measurements will be described in detail elsewhere (G.T.S. et al., unpublished data). In short, calibration relied on measuring the refractive indices of the droplets and cytosol and calibrating the stiffness using polystyrene beads in a fluid matching the droplet-to-cytosol index ratio. The corner frequency of the power spectrum of the bead position-as measured by a quadrant photodiode-was used to measure the trap stiffness. Since the trap stiffness experienced by a droplet also depends on its size, the stiffness was measured for beads of varying sizes that cover the range of sizes of lipid droplets ($\sim300 - 800$ nm). Lipid-droplet sizes were in turn measured by comparing their image in the differential interference contrast microscope to the images of polystyrene beads of known size immersed in a liquid to match the refractive index difference.

We performed the following control experiments that validate our conclusions on the value of forces reported in the main text:

a) To check that the video tracking method is capable of accurately measuring the stall forces of molecular motors, we used a typical bead assay (Vershinin et al., 2007) to measure the stall force of kinesin-1 in vitro the same way we do in vivo. The histogram of stall forces for

kinesin-1 is shown in Fig. S6A. The measured stall force for single motors is Gaussian distributed with an average of 4.2 pN, which is in good agreement with the value we measure using the more precise quadrant photodiode (4.6 pN) and the values reported in literature.

b) To check whether the calibration procedure for the trap stiffness gives the correct values in vivo, we purified lipid droplets (Cermelli et al., 2006) and suspended them in buffer. We then measured the average stiffness of the trap for such lipid droplets using the standard procedures used in vitro (Block et al., 1990; Mallik et al., 2004) and assuming a median diameter of the lipid droplets of 650 nm. This gave an average stiffness k = 4.3 ± 0.6 pN/100 nm. This value should be considered an upper limit on the stiffness experienced by droplets inside the embryo as all conceivable factors that may alter trap stiffness in vivo act to lower it (e.g. scattering from passing through the embryo, the slightly higher index of refraction of the cytosol than that of buffer). To use this maximum stiffness to estimate the forces in vivo, we plotted the distributions of stall distances contributing to the 2.6 pN and 5.2 pN peaks of Fig. 3C in the main text. As shown in Fig. S6B, the 2.6 pN peak is due to droplets that stall at distances (d) from the center of the trap distributed around ~ 62 nm. Using Hooke's law ($F = k \cdot d$) and a stiffness of k = 4.3 pN/100nm, this distribution of distances translates into stall forces peaked around 2.66 pN. The peak at 5.2 pN is due to lipid droplets stalling at distances centered around ~129 nm from the center of the trap, which translates into a stall force of 5.55 pN. These values are in excellent agreement with the values reported in the main text using the more careful, but elaborate procedure that accounts for the size of the individual lipid droplets being trapped and the index of refraction of the cytosol.

A two-sample Kolmogorov-Smirnov test (kstest2 function in the MATLAB (Mathworks, Natick, Massachusetts) package) was used to test whether the observed lipid droplet stall forces from wild-type and Khc^{27} heterozygous embryos were drawn from the same continuous distribution.

Supplemental References

Block, S.M., Goldstein, L.S., and Schnapp, B.J. (1990). Bead movement by single kinesin molecules studied with optical tweezers. Nature *348*, 348-352.

Carter, B.C., Shubeita, G.T., and Gross, S.P. (2005). Tracking single particles: a user-friendly quantitative evaluation. Phys Biol *2*, 60-72.

Cermelli, S., Guo, Y., Gross, S.P., and Welte, M.A. (2006). The lipid-droplet proteome reveals that droplets are a protein-storage depot. Curr Biol *16*, 1783-1795.

Culver-Hanlon, T.L., Lex, S.A., Stephens, A.D., Quintyne, N.J., and King, S.J. (2006). A microtubule-binding domain in dynactin increases dynein processivity by skating along microtubules. Nat Cell Biol *8*, 264-270.

Gindhart, J.G., Jr., Desai, C.J., Beushausen, S., Zinn, K., and Goldstein, L.S. (1998). Kinesin light chains are essential for axonal transport in Drosophila. J Cell Biol *141*, 443-454.

Gross, S.P., Guo, Y., Martinez, J.E., and Welte, M.A. (2003). A determinant for directionality of organelle transport in Drosophila embryos. Curr Biol *13*, 1660-1668.

Gross, S.P., Welte, M.A., Block, S.M., and Wieschaus, E.F. (2000). Dynein-mediated cargo transport in vivo. A switch controls travel distance. J Cell Biol *148*, 945-956.

Guo, Y., Jangi, S., and Welte, M.A. (2005). Organelle-specific control of intracellular transport: distinctly targeted isoforms of the regulator Klar. Mol Biol Cell *16*, 1406-1416.

Hill, D.B., Plaza, M.J., Bonin, K., and Holzwarth, G. (2004). Fast vesicle transport in PC12 neurites: velocities and forces. Eur Biophys J *33*, 623-632.

Kunwar, A., Vershinin, M., Xu, J., and Gross, S.P. (2008). Stepping, strain gating, and an unexpected force-velocity curve for multiple-motor based transport Current Biology *In Press*.

Kural, C., Kim, H., Syed, S., Goshima, G., Gelfand, V.I., and Selvin, P.R. (2005). Kinesin and dynein move a peroxisome in vivo: a tug-of-war or coordinated movement? Science *308*, 1469-1472.

Levi, V., Serpinskaya, A.S., Gratton, E., and Gelfand, V. (2006). Organelle transport along microtubules in Xenopus melanophores: evidence for cooperation between multiple motors. Biophys J *90*, 318-327.

Mallik, R., Carter, B.C., Lex, S.A., King, S.J., and Gross, S.P. (2004). Cytoplasmic dynein functions as a gear in response to load. Nature *427*, 649-652.

Martinez, J.E., Vershinin, M.D., Shubeita, G.T., and Gross, S.P. (2007). On the use of in vivo cargo velocity as a biophysical marker. Biochem Biophys Res Commun *353*, 835-840.

Müller, M.J., Klumpp, S., and Lipowsky, R. (2008). Tug-of-war as a cooperative mechanism for bidirectional cargo transport by molecular motors. Proc Natl Acad Sci U S A *105*, 4609-4614.

Palacios, I.M., and St Johnston, D. (2002). Kinesin light chain-independent function of the Kinesin heavy chain in cytoplasmic streaming and posterior localisation in the Drosophila oocyte. Development *129*, 5473-5485.

Pan, X., Ou, G., Civelekoglu-Scholey, G., Blacque, O.E., Endres, N.F., Tao, L., Mogilner, A., Leroux, M.R., Vale, R.D., and Scholey, J.M. (2006). Mechanism of transport of IFT particles in C. elegans cilia by the concerted action of kinesin-II and OSM-3 motors. J Cell Biol *174*, 1035-1045.

Petrov, D.Y., Mallik, R., Shubeita, G.T., Vershinin, M., Gross, S.P., and Yu, C.C. (2007). Studying molecular motor-based cargo transport: what is real and what is noise? Biophys J *92*, 2953-2963.

Saxton, W.M., Hicks, J., Goldstein, L.S., and Raff, E.C. (1991). Kinesin heavy chain is essential for viability and neuromuscular functions in Drosophila, but mutants show no defects in mitosis. Cell *64*, 1093-1102.

Schnitzer, M.J., Visscher, K., and Block, S.M. (2000). Force production by single kinesin motors. Nat Cell Biol *2*, 718-723.

Serbus, L.R., Cha, B.J., Theurkauf, W.E., and Saxton, W.M. (2005). Dynein and the actin cytoskeleton control kinesin-driven cytoplasmic streaming in Drosophila oocytes. Development *132*, 3743-3752.

Sisson, J.C., Field, C., Ventura, R., Royou, A., and Sullivan, W. (2000). Lava lamp, a novel peripheral golgi protein, is required for Drosophila melanogaster cellularization. J Cell Biol *151*, 905-918.

Vershinin, M., Carter, B.C., Razafsky, D.S., King, S.J., and Gross, S.P. (2007). Multiple-motor based transport and its regulation by Tau. Proc Natl Acad Sci U S A *104*, 87-92.

Welte, M.A., Cermelli, S., Griner, J., Viera, A., Guo, Y., Kim, D.H., Gindhart, J.G., and Gross, S.P. (2005). Regulation of lipid-droplet transport by the perilipin homolog LSD2. Curr Biol *15*, 1266-1275.

Welte, M.A., Gross, S.P., Postner, M., Block, S.M., and Wieschaus, E.F. (1998). Developmental regulation of vesicle transport in Drosophila embryos: forces and kinetics. Cell *92*, 547-557.

Supplemental Figures
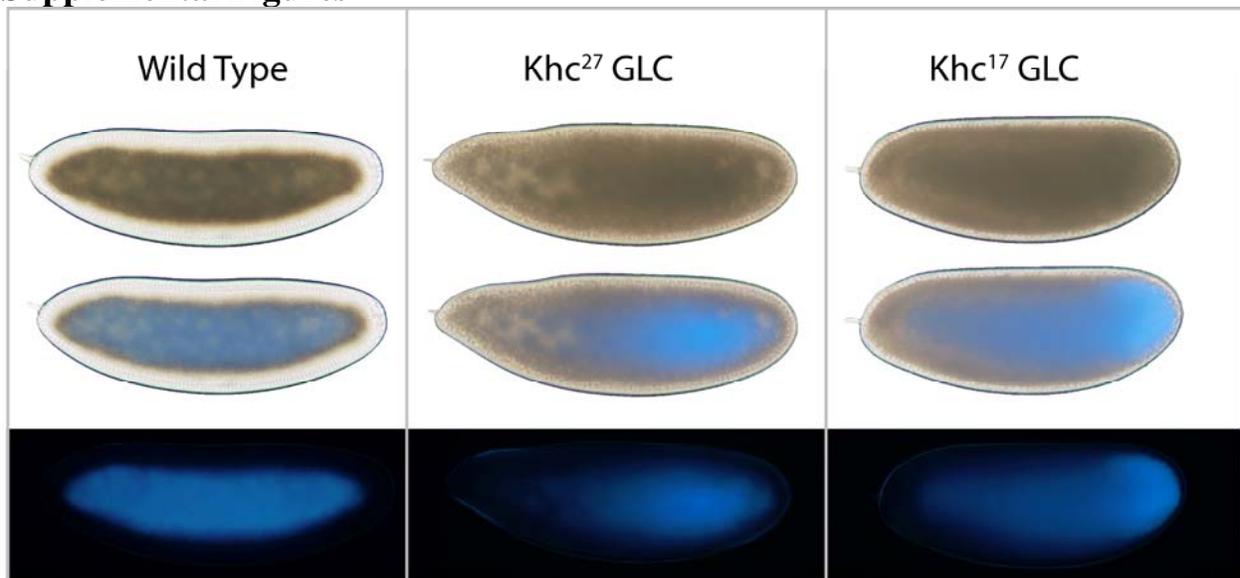
Figure S1

Fig. S1: Yolk vesicles display inward accumulation in *Khc* GLCs
Phase II embryos of various genotypes were inspected by bright-light microscopy (top) to reveal droplet distribution and by epifluorescence microscopy (bottom) to reveal the distribution of yolk vesicles (based on their autofluorescence). Middle panels: overlay of bright-light and fluorescence channels. Although lipid droplets remain peripheral (brown haze in bright-light images) in *Khc27* and *Khc17* GLCs, yolk vesicles are transported away from the surface, towards the center, like in the wild type. Note that yolk transport did not occur at the posterior end of this particular *Khc17* GLC embryo, presumably because of the localized microtubule defects when Khc function is impaired.

A 1 ½ ¼ Khc

D

Khc$^+$/Khc$^+$ + 2x P[Khc$^+$]
Khc^{27}/Khc$^+$ + 1x P[Khc$^+$]
Khc$^+$/Khc$^+$ + 1x P[Khc$^+$]
Khc$^+$/Khc$^+$
Khc^{27} GLC + 1x P[Khc$^+$]
Khc^{27}/Khc$^+$
Khc^{27} GLC

150 —
100 —
75 —

50 —

37 —

Khc

B Ph0 PhI PhII PhIII
W K W K W K W K
Khc

W = WT
K = Khc^{27}/+

E

Khc^{23} GLC   Khc^{17} GLC
WT   WT   WT   GLC   GLC
Khc
2x   1x   0.5x   1x   1x

C W K
Dic
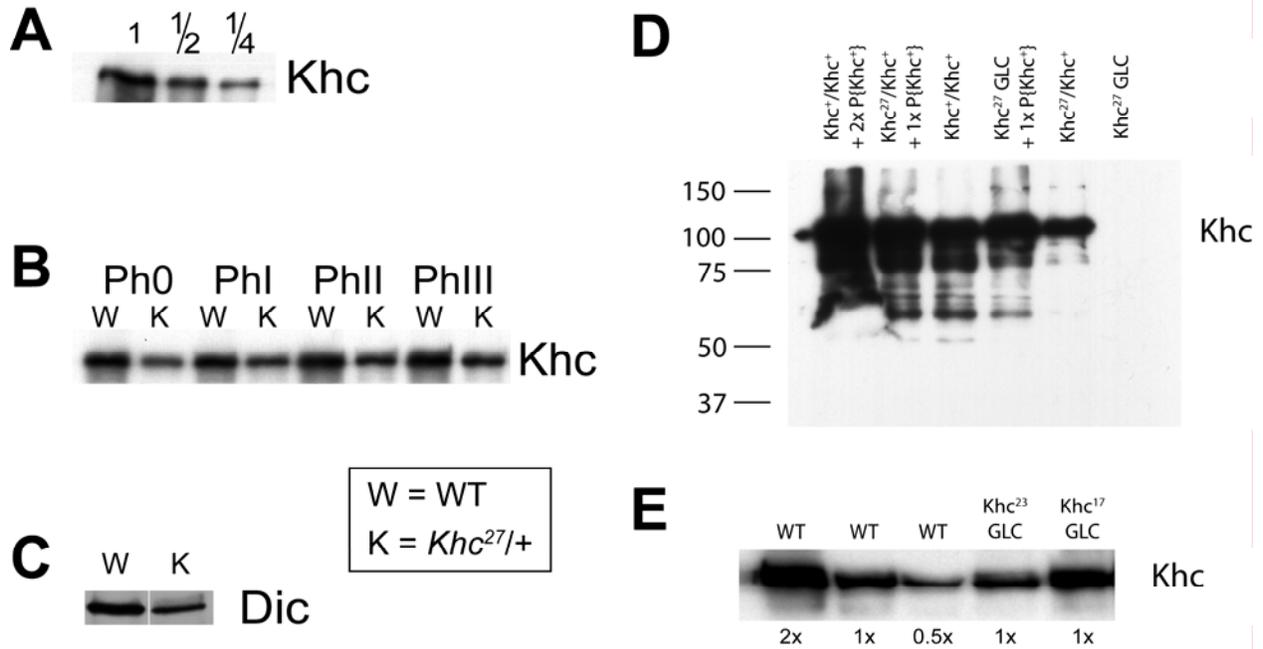
Figure S2

Fig. S2: Khc and Dic levels in various genetic backgrounds

A: Western analysis robustly detects two-fold differences in Khc levels. Protein extracts corresponding to decreasing numbers of Phase II wild-type embryos (1x = 10 embryos; 1/2x = 5 embryos; 1/4x = 2.5 embryos) were separated by SDS PAGE, transferred to membranes and analyzed with anti-Khc antibody.

B: *Khc^{27}/+* heterozygous embryos have reduced levels of Khc protein throughout all Phases of droplet transport. Proteins were extracted from wild-type or *Khc^{27}/+* heterozygous embryos in Phases 0, I, II and III (10 embryos/lane), and Khc was detected by western analysis. Coomassie Blue staining indicated equal loading. In a given genotype, Khc levels vary only slightly during development; Khc levels of *Khc^{27}/+* heterozygotes are always lower than in the wild type.

C: Dic levels on lipid droplets are reduced in the *Khc^{27}/+* compared to wild-type (WT) embryos. Lipid droplets were purified from the two genotypes, and equal amounts of total protein were separated by SDS PAGE and analyzed for the presence of the Cytoplasmic Dynein subunit Dic by western blotting. In repeated experiments, Dic levels on droplets from *Khc^{27}/+* embryos were consistently lower, though the absolute differences varied between trials.

D: The Khc antibody is specific for Khc. Long exposure of the western shown in Fig. 1B. Coomassie staining of membranes indicated equal loading across lanes (10 embryos per lane, data not shown). In addition to the main Khc band above 100 kDa, additional bands are visible in the wild-type (*Khc$^+$/Khc$^+$*) lane. These bands are apparently all derived from Khc (possibly degradation products) since they are absent in the *Khc^{27}* GLCs and because their intensity decreases as *Khc* dosage is lowered. Thus, the antibody does not recognize other proteins under

13

these conditions. In particular, note that in the *Khc²⁷* GLCs lane there are no cross-reacting bands in the molecular weight range 76-88 kDa (where the subunits of kinesin-2 migrate).
E: Khc is abundantly expressed in *Khc¹⁷* and *Khc²³* GLC embryos. Proteins were extracted from wild-type (WT) and *Khc¹⁷* and *Khc²³* GLC Phase II embryos, and Khc was detected by western analysis (2x = 20 embryos/lane; 1x = 10 embryos/lane; 0.5x = 5 embryos/lane).
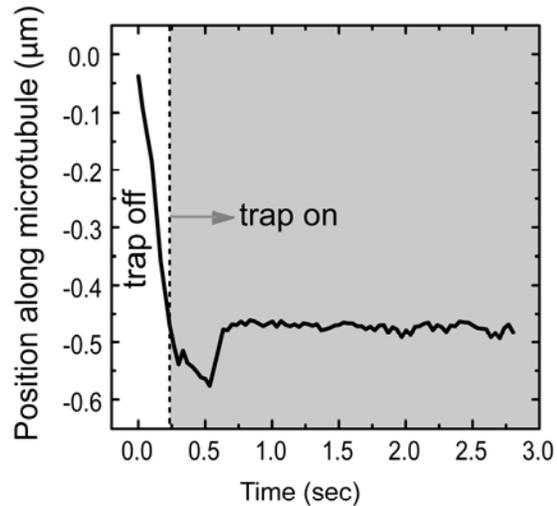
Figure S3

Fig. S3: Example of trace showing detachment of droplet before stalling
The lipid droplet moving steadily in the minus-end direction was trapped. This slowed it down, but the motors detached from the microtubule before stalling, making the droplet fall back to the center of the trap. This event would not be counted as a stall.
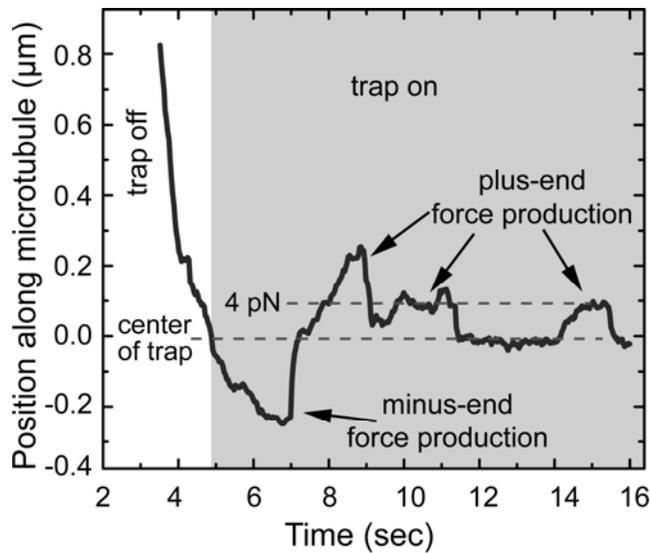
Figure S4

Fig. S4: Both polarity motors are simultaneously present on lipid droplets
The lipid droplet moving steadily in the minus-end direction was trapped which slowed it down. The minus-end motors finally detached, causing the droplet to fall back to the center of the trap. At that point (at 7.5 seconds) plus-end motors started pulling the droplet in the other direction, stalling and detaching a few times, as if trying to pull the droplet out of the influence of the trap. The rapid switching between plus-end and minus-end force production in the trap suggests that both polarity motors are simultaneously present and functional on the cargo.

15
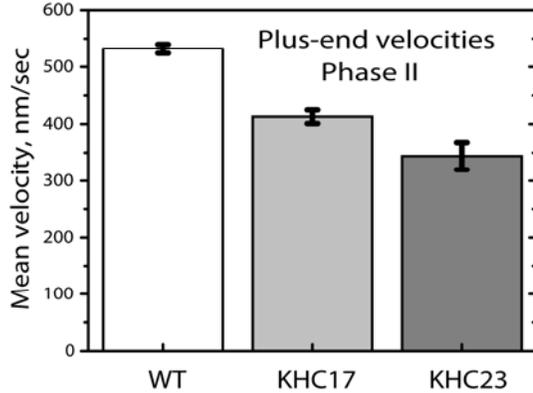
Figure S5

Fig. S5: Partial impairment of kinesin-1 results in allele-specific reductions of droplet velocity

Mean travel velocities of plus-end droplet motion were determined for wild-type, Khc^{17} GLC and Khc^{23}GLC embryos in Phase II. Two-sided rank-sum tests suggest that velocities are different between all three genotypes (p-value = 0.032 for $Khc23$ GLC versus $Khc17$ GLC, 1.4e-7 for $Khc23$ GLC versus wild type, and 2.6e-21 for $Khc17$ GLC versus wild type). For this calculation of average velocities, we employed runs longer than 350 nm (rather than runs longer than 500 nm as in Fig. 5E). For the wild type, this choice does not significantly affect the estimate of velocity: it is 532 ± 8 nm/s, when runs longer than 350 nm are used, and 554 ± 9 nm/s, when runs longer than 500 nm are used. For the mutants, this choice improves the statistical power of the analysis since in these genotypes runs longer than 500 nm are very rare (number of long runs on which velocity measurements are based: $n_{WT, >350nm} = 493$, $n_{WT, >500nm} = 379$, $n_{Khc17\,GLC} = 222$, $n_{Khc23\,GLC} = 22$).

A

B
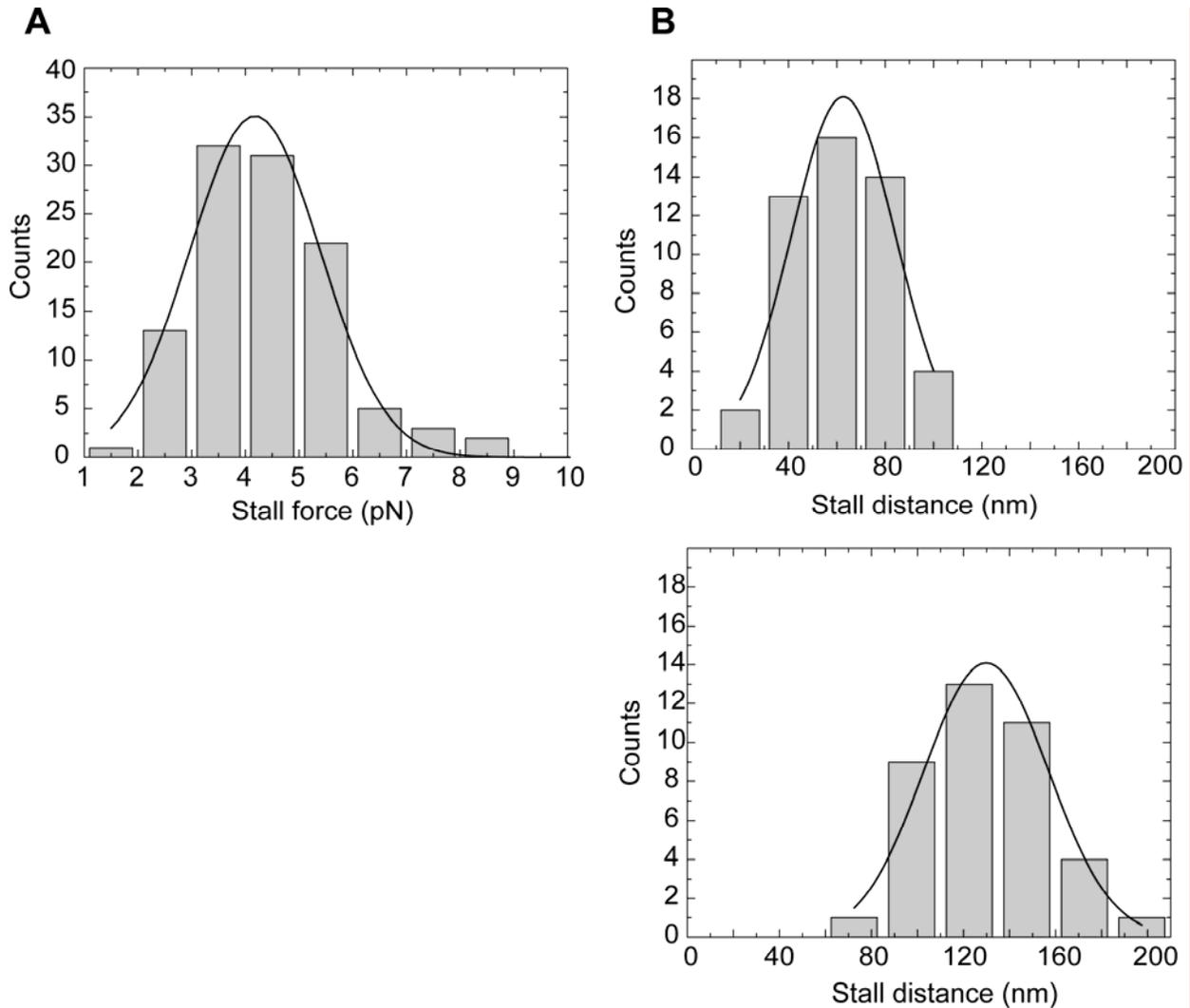
Figure S6

Fig. S6: Control experiments for trap stiffness calibration

A: Distribution of stall forces for kinesin-1 attached to polystyrene beads measured in an *in-vitro* bead assay as described in (Vershinin et al., 2007), but measuring bead motion in the trap by tracking its position from the video record rather than using a quadrant photodiode. The distribution is centered at 4.2 pN, which is in excellent agreement with the value of 4.6 pN measured using the quadrant photodiode for the same assay (data not shown). This demonstrates that the use of the video record enables us to measure forces in vivo.

B: Distribution of stall distances contributing to the two peaks in the plus-end stall force histogram in Fig. 3C (top: 2.6pN peak, bottom: 5.2pN peak). The center of the distributions gives the average stall distances which when multiplied by the average trap stiffness experienced by purified droplets, results in the average stall force for the two peaks. These values are in

excellent agreement with the values reported in Fig. 3C in the main text (see Experimental Procedures for details).